Intracellular stresses in patterned cell assemblies

Michel Moussus, Christelle C. Der Loughian, David Fuard, Marie Courçon, Danielle Gulino-Debrac, Hélène Delanoe-Ayari, Alice Nicolas

Intracellular stresses in patterned cell assemblies

Michel Moussus,[a] Christelle der Loughian,[b] David Fuard,[a] Marie Courçon,[c] Danielle Gulino-Debrac,[c] Hélène Delanoë-Ayari*[b] and Alice Nicolas*[a]

Confining cells on adhesive patterns allows performing robust, weakly dispersed, statistical analysis. *A priori,* adhesive patterns could be efficient tools to analyze intracellular cell stress fields, in particular when patterns are used to force the geometry of the cytoskeleton. This tool could then be very helpful in deciphering the relationship between the internal architecture of the cells and the mechanical, intracellular stresses. However, the quantification of the intracellular stresses is still something delicate to perform. Here we first propose a new, very simple and original method to quantify the intracellular stresses, which directly relates the strain the cells impose on the extracellular matrix to the intracellular stress field. This method is used to analyze how confinement influences the intracellular stress field. As a result, we show that the more confined the cells are, the more stressed they will be. The influence of the geometry of the adhesive patterns on the stress patterns is also discussed.

1 Introduction

Measuring cell contractility is emerging as an efficient tool to address intracellular mechanotransduction in various contexts, such as stem cell differentiation or vascular homeostasis.[1–3] Historically, this was performed by quantifying the expression of specific proteins, as myosin II or Rho activation pathways.[4–6] Recent advances in designing molecular Fluorescence Resonance Energy Transfer (FRET) sensors have permitted to get highly resolved maps of intracellular stresses through the deformation of optically resonant complexes bound to targeted entities such as proteins or lipids.[7,8] In addition to the experimental difficulties associated with the design of the optical probe, the transfection of the cells and image analysis, the FRET relevance relies on the right choice of the molecular target. A cruder quantification of cell intracellular stress maps that is not based on biochemical prerequisites would surely be an appreciable step in optimizing the FRET relevance. Direct mechanical measurements of cell intracellular stresses could in principle achieve this task.[9,10] Although less resolved than FRET, they offer stress maps that integrate the contribution of all the molecular partners, irrespective of their contribution to specific signaling pathways. An important issue is then to correlate the stress maps with the internal organization of the cells. However, getting stress maps using mechanical measurements is not routine yet, and requires difficult analysis steps.[10] One of the key issues is to take care of the boundary conditions when dealing with monolayers.[11] One strategy to circumvent this difficulty is to work with cell islands, confined on adhesive patterns.[12]

Adhesive patterns proved their efficiency to limit the variability in cell shape, either when isolated or in small assemblies.[13,14] Using patterns then allows to obtain a large amount of data on cell behavior and to correlate it with some geometry induced intracellular organization.[15] Consequently, patterns begin to be used as tools to probe intercellular forces and intracellular stresses.[12,16] Getting intracellular stress maps is presently being explored. Indeed, resolving the average intercellular forces in cell doublets is straightforward using a simple force balance argument.[16,17] On the other hand, determining local intracellular stresses presently relies on heavy mathematical calculations.[10] Then at the present time, the efficiency of using adhesive patterns to correlate the internal architecture of the cell with the mechanics is limited by the difficulty of calculating local stress maps.

In the present article, we propose a very simple and new method to calculate the local, internal cellular stresses, based on the derivation of the displacement field in the substrate that results from the transmission of the adhesion mediated cellular forces. We show that this method is valid whatever the size of the cell island, from isolated cells to monolayers. Limitations arise from the spatial resolution of the measurement of the bidimensional displacement field at the surface of the deformable substrate. We use this method to analyze the impact of confining cellular assemblies on adhesive patterns on the intracellular stress maps. In the first part, we present in detail this method. We then calculate stress maps for confined cell islands or monolayers, and discuss to what extent adhesive

[a]*LTM c/o CEA Léti, Université Joseph Fourier, CNRS UMR 5129, 17 av des Martyrs, F-38054 Grenoble cedex, France. E-mail: alice.nicolas@cea.fr*

[b]*Institut Lumière Matière, UMR5306 Université de Lyon 1-CNRS, Université de Lyon, 69622, Villeurbanne cedex, France. E-mail: helene.delanoe-ayari@univ-lyon1.fr*

[c]*Université Joseph Fourier, INSERM U1036, Commissariat à l'Energie Atomique et aux Energies Alternatives (CEA), Dpt des Sciences du Vivant (DSV), Institut de Recherches en Technologies et Sciences du Vivant (iRTSV), F-38054 Grenoble, France*

patterns are interesting tools to study cell mechanics. This analysis is performed with human umbilical vein endothelial cells (HUVECs). Actin networks in endothelial cells remodel as a cortical cortex when they reach confluence, unlike epithelial cells that maintain bundles of actin linked to focal contacts at their basal surface.[18,19] Probably related is the observation that endothelial cells get insensitive to the mechanical properties of the extracellular matrix when they reach confluence,[20] while epithelial cells do not.[21] Endothelial cells then appear as a model system when focusing on the intracellular stresses that originate from cell/cell contacts.

2 A new method to calculate intracellular stress maps

2.1 State of the art

Calculating mechanical stress maps has emerged as an important tool after it has become clear that mechanical distortion of the cell cytoskeleton could profoundly affect cell behavior.[22] The first approach, based on Butler *et al.*'s work,[9] quantifies average intracellular stresses. It balances the internal cellular stresses that apply on any closed contour sketched inside the cell assembly, with the cell/matrix forces integrated over the area that is enclosed by this contour.[23] Focused on the estimation of average quantities, it is designed for isolated cells or cellular assemblies where the field of observation is larger than the cellular assembly.[12,23,24] Then the calculation of the cell/matrix forces can safely be performed and does not rely on controversial approximations.[11,24] When local intracellular stresses are focused, local equilibrium must be addressed. Tambe *et al.*[10,11] proposed a direct calculation of the internal elastic stresses, based on the resolution of the elastic equations of a thin elastic sheet stressed by external, surface forces. Although in the biological problem intracellular stresses give rise to surface, adhesion mediated, stresses that strain the extracellular matrix, the linearity of the elastic equations justifies to turn the problem around and calculate the internal stresses as a result of known surface stresses. Using this method, the authors could, for the first time, derive a map of the intracellular stresses at play in an expanding epithelial cell sheet. In principle, the issue of calculating mechanical, intracellular stresses was solved. There is however an important technical limitation to this approach. As the first step, there is a need to calculate the forces that the cells transmit to the extracellular matrix. This calculation is very sensitive to the experimental noise[25] and to the boundary conditions.[11] This makes it necessary to work with large fields of view, and as a consequence small magnifications, to circumvent the impact of the undefined boundary conditions on the calculated force field. This in turn limits the resolution of the measurement of the displacement field, which increases the experimental noise and worsens the resolution of the calculated cell/matrix force field. This latter quantity is then substituted in the elastic equations to determine the local, intracellular stresses. As a whole, in addition to the mathematical heaviness of this multi-step approach, estimating the error in the quantification of the mechanical, intracellular stresses is far from simple.

2.2 Single cell contractility can be assessed through 2D deformation of the extracellular matrix

We here show that cell intracellular stresses can be assessed by a direct derivation of the displacement field at the surface of the extracellular matrix.

We consider either isolated adhering cells or cells organized in larger islands or in monolayers. In the following, the term "cell assembly" will refer to any of these cellular systems. Regarding any of them, their thickness h is small compared to their lateral extent L. As a consequence, stresses of small amplitude applied at the surface of the cell assembly will result in large internal strains.[26] For instance, a local in-plane surface force leads to compressive/expanding strains with amplitude EL/h being larger than the surface stress, where E is the Young's modulus of the cellular assembly.[27] Similarly, a small normal force bends the cell assembly and leads to large compressive/expanding strains away from the mid plane in the cellular assembly. This geometric property allows use of the thin elastic sheet assumption to compute the internal stresses.[26]

Intracellular stresses transmit stresses to the extracellular matrix. The displacement field that is measured at the surface of an elastic substrate gives information on these stresses. Since the displacement field is continuous at the interface between the cell assembly and the substrate, we also know the displacement field at the basal surface of the cell assembly. Experiments show that the displacement field has in-plane and out-of-plane components.[28–30] *A priori*, we could expect that they originate from in-plane or out-of-plane internal stresses. Would it be a net component of out-of-plane intracellular stresses when integrated over cell thickness, would the cell assembly bend at this location, therefore resulting in compressive/expanding in-plane intracellular stresses away from the mid plane of the bent cell assembly. As the cell assembly fills the thin elastic sheet approximation, we know that the amplitude of the in-plane intracellular stresses dominates the out-of-plane stresses. As a result, the intracellular stress fields are dominated by the in-plane components, σ_{ij}, with i and j referring to x or y (Fig. 1). Within the thin elastic sheet approximation, they are uniform in the thickness of the cell and simply can be written as[26]

$$\sigma_{xx} = \frac{E}{1-\nu^2}\left(\frac{\partial u_x}{\partial x} + \nu\frac{\partial u_y}{\partial y}\right)$$

$$\sigma_{yy} = \frac{E}{1-\nu^2}\left(\frac{\partial u_y}{\partial y} + \nu\frac{\partial u_x}{\partial x}\right)$$

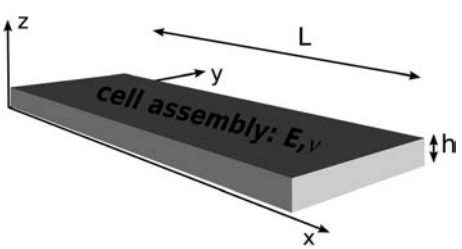

Fig. 1 Cellular assemblies are viewed as a thin elastic layer of Young's modulus E and Poisson's ratio ν.

$$\sigma_{xy} = \frac{E}{2(1+\nu)}\left(\frac{\partial u_x}{\partial y} + \frac{\partial u_y}{\partial x}\right) \quad (1)$$

where E and ν in eqn (1) are the Young's modulus and the Poisson's ratio of the cell assembly and need not be uniform. Neither out-of-plane components nor out-of-plane derivatives of the displacement field enter in eqn (1) due to the thin sheet elastic approximation. Then calculating the intracellular stresses becomes experimentally very easy. Bidimensional measurement of the elastic deformation of the extracellular matrix allows assessing the intracellular stress field, with no intermediate calculation of cell/matrix forces. This method is only limited by the resolution of the measurement of the deformation field.

2.3 Sensitivity to the experimental noise

Since no intermediate calculation of the forces that are transmitted to the extracellular matrix is performed, the sensitivity to the experimental noise of this one step method can be calculated from eqn (1):

$$\left(\frac{\Delta\sigma}{\sigma}\right)^2 \simeq \left(\frac{\Delta E}{E}\right)^2 + \left(\frac{\Delta\nu}{1-\nu}\right)^2 + \frac{1+\nu^2}{(1+\nu)^2}\left(\frac{\Delta(\partial u_x/\partial x)}{(\partial u_x/\partial x)}\right)^2 \quad (2)$$

Although the orientation of the stress tensor is not sensitive to the elastic constants of the cellular assembly (see eqn (1)), they do impact the stress amplitude. Scanning the elastic properties of cellular assemblies revealed that in the case of HUVECs, the Young's modulus varies from more than 100% when scanning from the center to the periphery of cellular assemblies.[31] Finite sized assemblies have a more dispersed distribution of Young's modulus than single cells or monolayers. Since we do not know the impact of confining cells on adhesive patterns on the spatial variation of the Young's modulus, we take the average value of $E = 1000$ Pa. Regarding the data obtained in ref. 31, this leads to a potential error on the stress amplitude of about 20%, larger errors being committed at the periphery of cell islands (30% error). Variations of the Poisson's ratio however impact the amplitude and the orientation of the stress tensor. In the absence of data, we take the value of $\nu = 0.5$ (incompressible cellular assembly). Variation of the Poisson's ratio down to 0.3 could induce an error as large as 13%. The last term in eqn (2) originates from the experimental errors in the measurement of the displacement field. In order to quantify it, we calculated the impact of adding a Gaussian noise to the displacement field. In our experiment, the noise on the displacement field is indeed Gaussian and of amplitude 0.75 pixels. This introduced an error term $\Delta(\partial u_x/\partial x)/(\partial u_x/\partial x)$ of less than 10%. As a whole, the error in our estimation of the intracellular stresses mainly originates from the unknown elastic properties of the cellular assembly, and ranges from 25% for a monolayer to almost 40% for cell islands. It is to be noted that the relative error drops down to less than 10% when comparing cellular assemblies of similar geometry, such as adhesive patterns or monolayers, where on average, the elastic constants could be considered as identical.

2.4 Validation of the method

Experimentally, we measure the 2D displacement field within the gel u_x, u_y. From these measurements, we can simply calculate the gradients of these quantities and thus calculate the stress using eqn (1). We describe the stress tensor by two quantities that are geometric invariants: the euclidian norm,

$$\|\sigma\| = \sqrt{\sum_{i,j} {\sigma_{ij}}^2} \quad (3)$$

and the deviator, which we define as the norm of the normalized deviatoric stress tensor:

$$\eta = \frac{\left\|\sigma - \frac{1}{2}\mathrm{tr}(\sigma) I_2\right\|}{\|\sigma\|} \quad (4)$$

where $\mathrm{tr}(\sigma)$ is the trace of the tensor and I_2 is the identity square matrix in 2 dimensions. η is a measure of the anisotropy of the stress tensor. It ranges between 0 and 1. $\eta = 0$ when the stress tensor is isotropic, and only contains hydrostatic pressure terms. $\eta = 1$ when the tensor is antisymmetric, its two eigenvalues being opposite. We tested the calculation of the intracellular stress tensor on an actin-labeled, isolated HUVE cell that migrates onto a fibronectin coated extracellular matrix. As shown in Fig. 2A, actin is organized as a large cortical cortex bordered by a narrow lamellipodium structure along its migrating front. Retracting filopodia are visible at the back edge of the cell.

The calculated stress gives us very different interesting information:

(1) The maxima of the amplitude of the stress tensor (Fig. 2D) colocalize with the maxima of the stress exerted by the cell on the matrix (Fig. 2G), which are themselves well colocalized with adhesive patterns (bright actin structure in Fig. 2A). This is not surprising as for a single cell the contractile activity of the actin network needs to be transmitted to the surface through the adhesive sites.

(2) It also reveals much finer behaviors, invisible in the force field, through the deviator map: this shows regions where the amplitude of the stress is small, but anisotropy is important: this colocalizes with edges of the cells where polymerization/depolymerization activity is important due to the movement of the cell (which moves here from the top to the bottom of the field of view).

(3) In addition, the main directions of the stress tensor partially correlate with the orientation of the actin fibers that are observed in the basal plane of the cell (Fig. 2C). Full agreement (confined distribution around 0 or 90 degrees) would be expected in case cell contractility would exclusively be directed by actomyosin fibers located at the basal plane of the cell. Although they undoubtedly contribute to the intracellular forces, out-of-plane contractile actomyosin fibers have been described, which are not accounted here.[33] The validation of our method can therefore only be done at the periphery of the cell, where no out-of-plane contractile machinery is present. As can be seen in Fig. 2B, the orientation of the stress tensor then fully correlates with actin extensions.

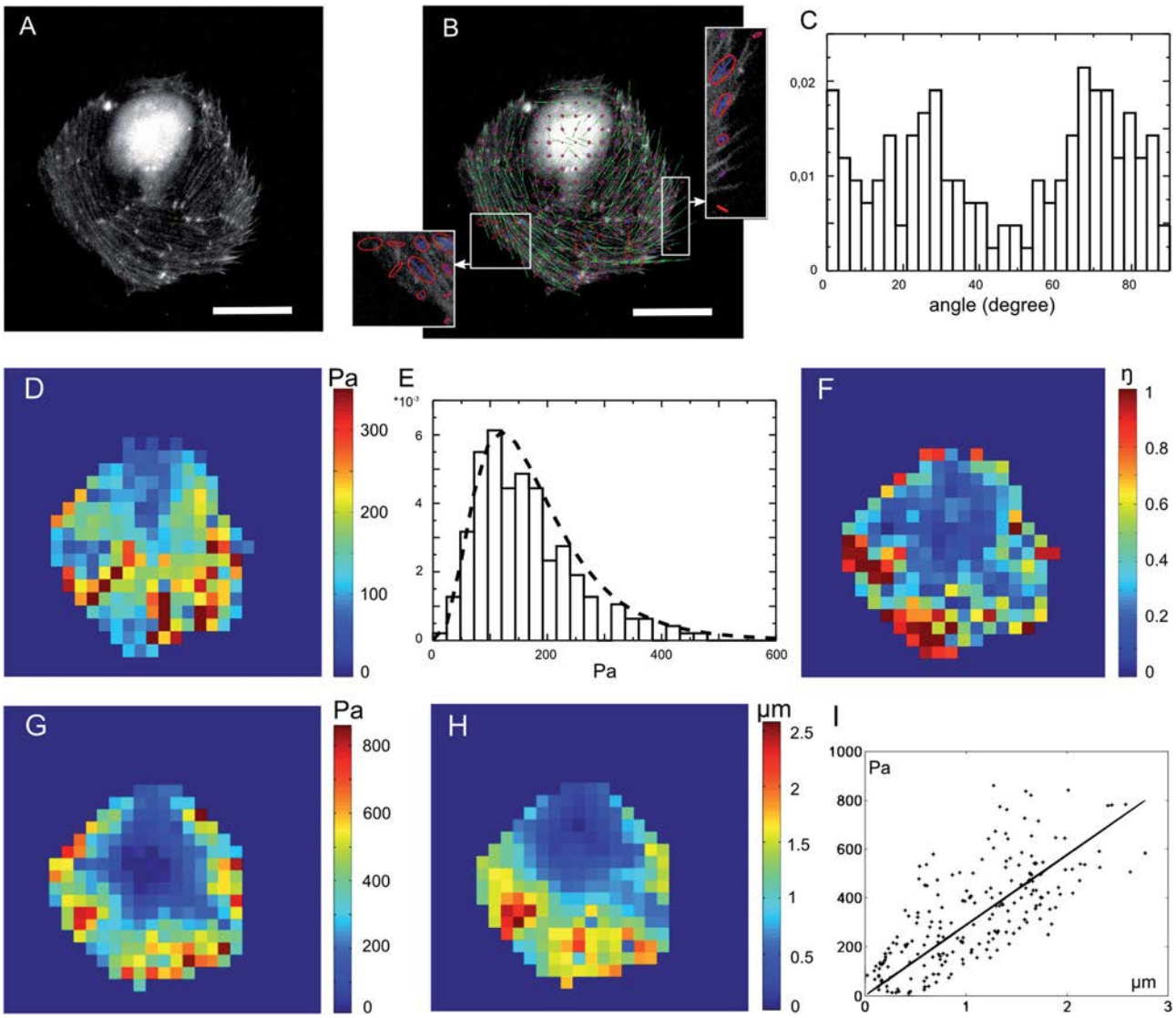

Fig. 2 Calculated stress in an actin labeled, migrating HUVE cell. (A) HUVE cell stained for actin. (B) Representation of the stress tensor in its eigenbasis. The lengths of the axes of the ellipses are given by the norm of the eigenvalues of the stress tensor. Negative eigenvalues are labeled in blue. Actin fibers (green lines) are detected by Fourier analysis (see Material and methods). (C) Deviation angle between the detected actin fibers and the major axis of the stress tensor. (D) Amplitude map and (E) histogram of the amplitude of the stress tensor. The estimated most probable stress is of the order of 100 Pa. (F) Deviator map of the stress tensor. (G) Amplitude map of the stress field exerted by the cell on the extracellular matrix calculated as in ref. 32. (H) Amplitude map of the displacements under the cell. (I) Correlation between G and H. Bar 20 μm.

3 Results

We now use our original calculation method to analyze the intracellular stress fields in cell islands confined on adhesive patterns. Our aim is to elucidate whether pattern-induced confinement influences the stress field.

3.1 The intracellular stress pattern in patterned HUVECs does not reproduce the symmetry of the island

As shown in Fig. 3, the axisymmetry of the HUVEC island is not visible in the spatial distribution of the amplitude of the stress, nor in the anisotropy of the stress tensor. Large stresses can be found either at the periphery or in the center of the island. Regions of anisotropic stresses are spread through the island and do not localize preferentially at the periphery, as observed in single cells (Fig. 2). In addition, neither the spatial distribution of the amplitude nor of the deviator correlate with the cell contours inside the cellular assembly (data not shown).

3.2 But confinement enhances the amplitude of the cellular stresses

We analyzed the intracellular stresses in HUVEC islands grown on adhesive patterns of diameter 100 μm and 150 μm, and compared to intracellular stresses in monolayers. As for single cells (see Fig. 2), the maxima of the stress norm colocalize very well with the maxima of usual traction forces as calculated in ref. 34 (compare Fig. 3B and E). Moreover, we obtain the same orders of magnitude as the ones obtained by Krishnan *et al.*[12] in islands

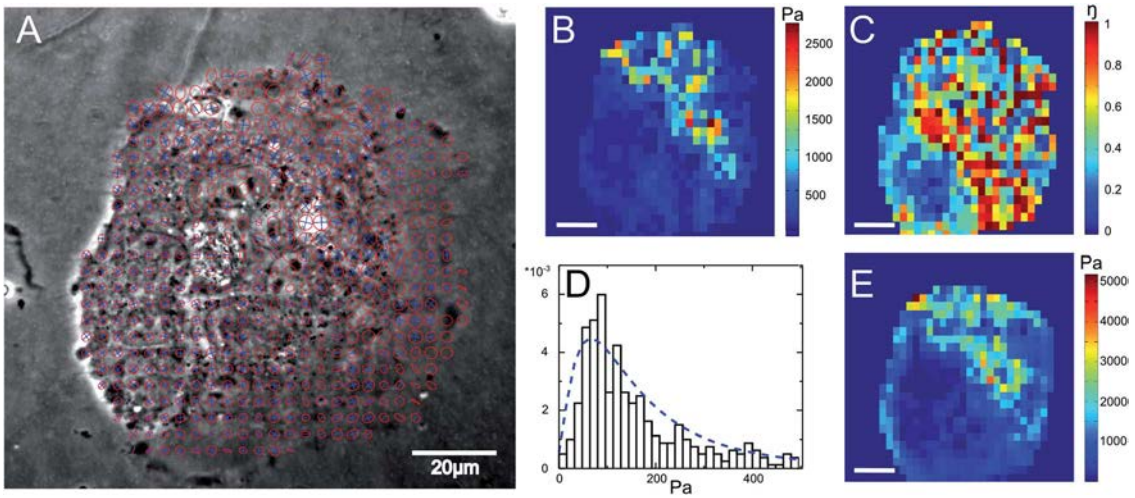

Fig. 3 Intracellular stress distribution in a HUVE cell island on a 100 µm adhesive pattern. (A) Phase contrast image of the cell island with superimposed ellipses that show the orientations of the stress tensor. Blue axes stand for negative eigenvalues, and no axis is drawn when the eigenvalue is positive. The length of the axes scales with the log of the norm of the stress tensor. (B) Spatial distribution of amplitude of the stress tensor. (C) Spatial distribution of the deviator η. (D) Histogram of the norm of the stress tensor, fitted by a log-normal distribution. The estimated most probable stress is 50 Pa. (E) Amplitude map of the stress field exerted by the cell on the extracellular matrix calculated as in ref. 32. Bar: 20 µm.

of endothelial cells. However, stresses in a cell assembly are not only coming from cell–substrate interactions, but also from cell–cell interactions. So as a marker of cell contractility, we chose not to use the maxima of the stresses (which seem to be associated with cell substrate interactions), but the most probable value of this stress in a monolayer, as given by the maximum of the fit of the stress distribution by a log-normal distribution (see Fig. 3D). This is this specific measurement that we compare between cell islands and cell monolayers. As shown in Fig. 4, we observe that the amplitudes of both the displacement field measured under the islands, at the top of the extracellular matrix, and the intracellular stress field in the islands are sensitive to the finite size of the islands. Consistently, intracellular stresses are even larger in isolated cells, as shown in Fig. 2F with a most probable value of about 100 Pa. Smaller cellular assemblies therefore appear to transmit larger stresses to the extracellular matrix and to feel larger intracellular stresses.

We also checked that chemical inhibition of cell contractility reduces cell mechanical stresses. Cellular assemblies were treated with blebbistatin at a concentration of 25 µM. The stresses were measured 5, 15 and 25 min after the addition of the drug. We observe that both the amplitudes of the displacement field and of the intracellular stresses drop dramatically (Fig. 4A and B). In the absence of data concerning the effect of blebbistatin on the elastic properties of the cellular assemblies, the estimation of the stress field is done with keeping a constant value for the Young's modulus. Considering that blebbistatin also remodels the cytoskeleton and makes the cells softer would enhance the observed trend.

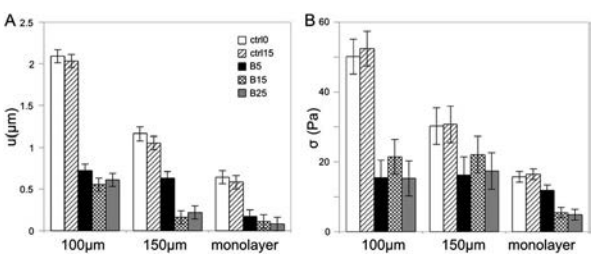

Fig. 4 Confinement effects on displacement and stress fields. Most probable (A) displacement and (B) stress amplitudes, on 100 µm, 150 µm adhesive patterns, and for a monolayer. Ctrl0 and Ctrl15 correspond to images taken at 0 and 15 min. Releasing cell contractility by the addition of blebbistatin is observed 5 (B5), 15 (B15) and 25 (B25) min after the addition of the drug.

3.3 The displacement field propagation is highly influenced by the finite size of the patterned islands

We also study the correlation length of the fluctuations of the displacement field:

$$(\widetilde{u}_1, \widetilde{u}_2) = (u_1(x,\ y) - \langle u_1 \rangle,\ u_2(x,\ y) - \langle u_2 \rangle),$$

which accounts for the stresses the cells exert on the extracellular matrix, using

$$C(x_0, y_0) = \frac{\int \sum_i \widetilde{u}_i(x + x_0, y + y_0)\widetilde{u}_i(x, y)\mathrm{d}x\mathrm{d}y}{\int \sum_i \widetilde{u}_i(x, y)^2 \mathrm{d}x\mathrm{d}y} \qquad (5)$$

The correlation image is then interpolated on a polar mesh and averaged over all angles. We thus obtain the curve $C(d)$, which can be fitted by a decreasing exponential giving access to the correlation lengths λ_u, whose values are summarized in Table 1. We see that the correlation length increases with the size of the cell ensemble. Fig. 2I shows that the displacement field and the stress field exerted on the substrate are proportional under the cell, so their patterns have similar sizes. We can conclude that the characteristic size of cell/matrix stress patterns is about $2 \times \lambda_u \approx 60$ µm in HUVEC monolayers (Table 1). It is therefore not

surprising that islands of the order of a few hundreds of microns in diameter feel finite size effects.

3.4 The intracellular stress propagation is also influenced by the finite size of the patterned islands

The intracellular stresses propagate over a very short distance inside HUVEC islands, as quantified by the exponential decay of the average cross-correlation function (Fig. 5A):

$$C(x_0, y_0) = \frac{\int \sum_{(i,j)} \sigma_{ij}(x + x_0, y + y_0)\sigma_{ij}(x, y)\mathrm{d}x\mathrm{d}y}{\int \sum_{(i,j)} \sigma_{ij}(x, y)^2 \mathrm{d}x\mathrm{d}y} \quad (6)$$

We calculate eqn (6) for the fluctuations of the stress tensor, $(\sigma(x,y) - \langle\sigma\rangle)$, where $\langle\sigma\rangle$ is the average stress tensor, so that the mean value of the stress tensor does not flatten the correlation profile. Table 1 shows that the correlation length of the stress increases with the size of the cell population studied. However, we want to pinpoint that we have reached values close to our resolution limit, so to go further even higher imaging resolution would be required.

In order to get a finer view of the impact of the geometry on the stress distribution, we performed the angular cross-correlation of the stress tensor:

$$C(r, \theta) = \frac{\int \mathrm{d}\theta' \sum_{(i,j)} \sigma_{ij}(r, \theta' + \theta)\sigma_{ij}(r, \theta')}{\int \mathrm{d}\theta' \sum_{(i,j)} \sigma_{ij}(r, \theta')^2} \quad (7)$$

As previously discussed, the angular cross-correlation is calculated for the fluctuations of the stress tensor.

It is revealed that a structured organization is easily noticeable in cell islands. Indeed, anti-correlation is visible close to the center of the island (Fig. 5B). This reveals that the stress field changes orientation in a correlated way along inner circles. When one moves to outside circles, one can observe that the anti-correlation decreases in amplitude and increases in its number of minima, meaning that the change in the orientation of the intracellular forces occurs on shorter angular openings and is less and less visible when moving away from the center of the island.

4 Discussion

We propose here a simple, one step, original method to quantify intracellular stresses. Compared to existing methods, the major advantages of this method are that (i) it is not sensitive to the lack of knowledge of the stresses out of the field of view and (ii) the elastic properties of the cellular assembly do not need to be uniform. In addition, the accuracy of the calculated stress field can be easily estimated from the experimental errors (eqn (2)) and does not need extensive computational tests. As discussed in Section 2, the major source of inaccuracy comes from the lack of knowledge of the elastic properties of the cellular assembly. This limits the ability of making comparison on the magnitude of intracellular stresses between distinct cytoskeleton architectures, for instance, when focusing on specific drug treatment. This can however be improved by coupling the stress quantification to the measurement of the elastic properties of the cells. This limitation is shared by the other methods to a similar extent,[10,11,23] since they also require strain/stress conversion in the course of the calculation. Nevertheless, relative variations of the amplitude of the stress field are attainable with a much better accuracy when the elastic properties of the cellular assemblies are known to be similar, which is the case here when we compare cell islands and monolayers.[31] Then it is the resolution of the displacement field that fixes the error bar (less than 10% in our experiment). In addition, as previously mentioned, the orientation of the calculated stress field is only sensitive to the Poisson's ratio. Regarding the range of values of measured Poisson's ratios, between 0.3 and 0.5, the orientation of the calculated stress field is expected to be known in an absolute manner within 15% accuracy.

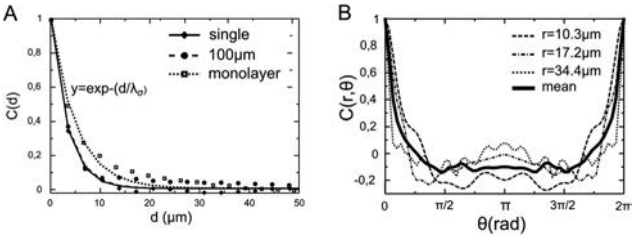

Fig. 5 Propagation of the intracellular stresses. (A) Intracellular stresses propagate over a micron scale length independent of the size of the cellular assembly. Correlation lengths are respectively 3.2 ± 0.2, 3.5 ± 0.3 and 5.7 ± 0.3 μm for isolated cells, 100 μm diameter island, and a monolayer. (B) Variation of the angular correlation function for different radii r in the 100 μm island, averaged over 2 time lapses. Anti-correlation is less apparent when r increases, revealing the disappearance of the organization of the stress as a dipole. The mean is performed through the entire island.

Table 1 Correlation lengths of displacements λ_u and stresses λ_σ

	Single cell	100 μm island	150 μm island	Monolayer
λ_u (μm)	9.3 ± 1.2	11.0 ± 0.9	17.5 ± 1.8	27.4 ± 0.6
λ_σ (μm)	3.2 ± 0.2	3.5 ± 0.3	4.0 ± 0.2	5.7 ± 0.3

A major result we find is that both the stress and the displacement amplitudes vary with the size of the cellular assembly. Consequently, both the intercellular forces and the forces the cells exert on the extracellular matrix are sensitive to the size of the cellular assembly. Within the range of sizes of patterns we studied, this effect does not result from edge effects that are concentrated at the periphery of the cellular assembly. The symmetry of the pattern is not visible in the stress field, neither in the spatial distribution of amplitude nor in the deviatoric tensor. Confining cellular assemblies on adhesive patterns therefore appear to limit edge effects, which are expected for a non-confined, growing cell island.[10]

One can ask, whether cell density (or equivalently cell spreading) has a role to play in the difference obtained here on

patterned and non-patterned surfaces. It has, indeed, already been shown that cell behavior and fate are influenced by the spreading area of cells.[35] To answer these questions, we also measured the cell density by our different experiments. Cell densities were indeed greater in cellular islands: 1.9×10^3 and 2.1×10^3 cells per μm^2 (islands of radius 100 μm and 150 μm respectively) *versus* 1.3×10^3 cells per μm^2 in cellular monolayers. These measurements were easily performed using images taken after adding trypsin to the sample, when cells can be easily counted, because they are well separated from each other (see ESI, Fig. 1†). Right now it is difficult to assess whether this is a cause or a consequence of an increased cellular contractility on the patterned substrate.

The stress amplitudes we estimated by our calculation compare with the ones that were reported for endothelial cells with other calculation methods.[10,11] However, we predict a much smaller characteristic range in which the stress patterns propagate (about 10 times smaller). A reason could be that we focus on stress patterns (and therefore stress tensor), while ref. 10 focused on the stress amplitude. Another reason could be that this quantity is sensitive to the resolution of the imaging, which, in our case is 6 times larger. Both in ref. 10 and in our work, the correlation length that is predicted is of the order of the size of the window that is used in the course of the measurement of the displacement field using particle imaging velocimetry. This would mean anyway that if we want to get a proper reconstruction of the stress field in a monolayer, it is then absolutely necessary to satisfy the Nyquist–Shannon criterium (the frequency of the sampling should be at least twice the highest frequency contained in the original signal). We showed that this frequency is higher than $1/\lambda_\sigma$. If we want to get real true and precise measurements of the stress field, we will have to go to resolutions even higher than the one used in our study.

We also find that confining cells on adhesive patterns impacts the propagation of cell/matrix forces inside the island. Cell/matrix forces are approximately proportional to the displacement field (see Fig. 2I), for which we showed that the correlation length increases when increasing the size of the cellular assembly. This result is expected since we show that patterns of the displacement field occur on about $2 \times \lambda_u = 60$ μm adhesive patterns (Fig. 4). Then cell islands with sizes of a few hundreds of microns are too small assemblies to limit the sensitivity to the edge effects. It is to be noted that the value we find for the correlation length of the displacement field is consistent with other measurements, performed on softer gels with epithelial cells.[36]

5 Conclusion

Confining cells on patterns has already proved its efficiency in performing well resolved, statistical analysis. However, we show that confinement impacts the amplitude of the intracellular stresses, as well as of the cell/matrix stresses. It also locally modifies the propagation of the intracellular stresses, as a result of the symmetry imposed by the pattern (Fig. 5). Only the core of the pattern, of 3 to 4 cells in 100 μm islands, transmits intracellular stresses in a similar manner to that for a monolayer. These perturbations, due to confinement effects, are with no doubt related to a distinct organization and/or activation level of the contractile machinery of the cells. Then it is uncertain that results obtained on confined assemblies will reflect the biochemical response of monolayers. In order to recover appropriate stress amplitudes and patterns, adhesive patterns should exceed 200 μm, and the analysis should be performed at the core of the pattern. Although it might limit the interest in using patterns, it still permits to organize a few cells (the core of the pattern) within a reproducible surrounding, and therefore allows to perform weakly dispersed statistical analysis with, as a cost, increasing the number of analyzed patterns.

6 Experimental section

6.1 Gel fabrication

30 mm glass slides were chemically activated using BindSilane (Fisher Scientific) to allow stable, covalent bonding of polyacrylamide hydrogels. The glass slides were first cleaned by immersing in a 0.1 M NaOH solution for 10 min. They were then rinsed in ethanol and dried using dry air. A solution containing 484 μl of acetic acid and 56 μl of BindSilane completed up to 15 ml with ethanol was prepared. 500 μl of this solution was pipetted to each glass slide and wiped off with a dust free wiper.

Polyacrylamide hydrogels were prepared with 8% acrylamide, 0.03% *N*,*N*-methylene-bis-acrylamide, ammonium persulfate (10% w/v solution, 1 : 125 volume), TEMED (1 : 1250 volume; all Bio-Rad products) and 0.22% v/v of 0.2 μm fluorescent beads (2% solid red beads, Molecular Probes). After 30 min of degassing, 30 μl of the mixture was poured onto the glass slide. A hydrophobic cover slide equipped with 40 μm thick wedges was deposited on the droplet. After polymerization (15–30 min), the hydrophobic cover slide was gently removed, and the gel was allowed to swell in distilled water for 24 h. The Young's modulus of the gel was measured as described in ref. 37. We found an average value of 5 ± 0.5 kPa. It is to be noted that the elastic constants of the gel do not enter in the calculation of the intracellular stresses. Only the elastic properties of the cells matter. The composition of the gel is optimized to get displacement amplitudes that allow easy handling of particle tracking (a few microns of average in-plane displacement, as few as possible out-of-plane displacement).

6.2 Uniform surface functionalization

Polyacrylamide gels were functionalized with a theoretical concentration of 5.4 μg cm^{-2} of fibronectin from human plasma (Roche Applied Science). Fibronectin was covalently attached to the surface of the gel using a photoactivatable heterobifunctional reagent named Sulfo-LC-SDA (Pierce). This reagent differs from the commonly used Sulfo-SANPAH[38] by its photosensitive group, a diazirine group, which is more stable and more reactive. A solution of 1.8 mg ml^{-1} of Sulfo-LC-SDA in PBS was prepared and kept protected from light. 1 ml of this solution was poured onto the surface of the gel in a dark room. After 2 hours, the solution was removed and replaced by the fibronectin solution for 1 h. After removing the fibronectin

solution, the gels were exposed to UV 365 nm light (18 mW cm^{-2}) for 5 min. The gels were then washed with PBS and incubated with cell culture medium 1 h before cell seeding.

6.3 Patterned surface functionalization

In order to get cell islands, polyacrylamide hydrogels were coated with circular patterns of fibronectin of different sizes. This was performed using PDMS membranes as covers.[39] PDMS membranes were prepared as follows (Fig. 6). Arrays of circles with varying diameters and spacings were designed using L-Edit software (Tanner Research, Inc.). The resulting layouts were then used to produce chrome/glass photolithographic masks. These patterns were then transferred into photoresist-coated silicon wafers using contact lithography. Following photoresist patterning, the resist was developed and the wafers were etched to a depth of 50 μm using deep reactive ion etching (Fig. 6B). The fabricated silicon molds were then used to cast PDMS, yielding negative impressions of the desired surface features. For this purpose, a bicomponent PDMS Sylgard 184 (Dow Corning) was used. The two PDMS components were thoroughly mixed using a 10 : 1 base to curing agent mixing ratio in mass. The PDMS was degassed under vacuum to remove bubbles produced during the mixing. The mixture was then poured onto the silicon molds and spin-coated to a thickness of 40 μm and finally cured for 1 h at 100 °C. After this step a thin layer of PDMS remained on top of the circular patterns and it was removed by selective PDMS etching.[40] Tweezers were used to unmold the thin PDMS membrane and bring it in contact with the gel surface (Fig. 6C). Surface functionalization was then performed, as previously, on the gel covered by the PDMS membrane.

6.4 Cell culture

Low-passage (P2–P3) human umbilical vein endothelial cells (HUVECs) were grown in EBM-2 medium supplemented with EGM-2 SingleQuots (Lonza). The cells in islands were seeded at a density of 10^4 cells per cm^2 and allowed to adhere to the gel for 1 h at 37 °C and 5% CO_2. The PDMS membrane was then carefully peeled off. Experiments were conducted 24 h after cell seeding. Cells in monolayers were seeded at a density of 5×10^4 cells per cm^2. In the case of monolayers, experiments were conducted 48 h after cell seeding.

Actin labeling was performed using nucleofection (Amaxa Biosystems) according to the manufacturer's protocol. Briefly, the day before transfection, the cells were seeded at a density of 3×10^4 cells per cm^2 in EBM-2 medium supplemented with EGM-2 SingleQuots. For each plasmid transfection, 2×10^6 cells were harvested using Reagent Pack (Cambrex) and pelleted by centrifugation (6 min at 1000 rpm) prior to being resuspended in 100 μl of Nucleofector® solution, mixed with 4 μg of GFP-LifeAct plasmid, a gift from Roland Wedlich-Söldner (Max Planck Institute for Biochemistry) and subjected to nucleofection. Plasmid-transfected cells were seeded at 3000 cells per cm^2 on the gels and used 24 h after transfection.

6.5 Limitation of cell contractility

Blebbistatin (Calbiochem) was prepared as a 50 mM stock solution in dimethyl sulfoxide (DMSO) and used at a concentration of 25 μM. The culture medium was replaced 1 hour before the addition of blebbistatin. Blebbistatin treatment consisted of replacing half of the culture medium contained in a 35 mm diameter dish (1 ml) with the same volume of blebbistatin diluted at the final concentration. Observations were conducted 5, 15 and 25 min after the addition of blebbistatin.

6.6 Image acquisition

Single-field images, of size 1344 × 1024 pixels, were collected using an IX71 inverted Olympus microscope equipped with a heating work plate, a humidifier, and a CO_2 delivery system. The acquisition was performed using a UPlan FLN x60/1.25 Ph3 oil objective and an ORCA-ER camera (Hamamatsu). Four field images, of size 2560 × 2160 pixels, were collected using a Leica inverted microscope DMIRB, equipped with a Neo camera (Andor). Both microscopes were equipped with a motorized stage for precise z acquisitions.

For every position, three types of images were collected: (i) a phase contrast image of the cells, (ii) a stack of 12 fluorescence images of the beads located immediately below the cells ($\Delta z = 0.3$ μm) and (iii) a stack of 5 fluorescence images of the layers of beads in contact with the glass slide ($\Delta z = 0.5$ μm). The stack at the surface of the gel allowed selection of the same plane of beads whatever the drug treatment and the resulting large deformations of the gel. The stack at the bottom of the gel was used to correct the three-dimensional drift of the microscope. At the end of the time course experiment, cells were trypsinized using 1x trypsin (Lonza) to get reference images of the surface of the gel in the absence of a force load.

6.7 Detection of surface deformation and force calculation

Stacks were aligned at the subpixel resolution in the xy and z direction using image correlation with Matlab software. We

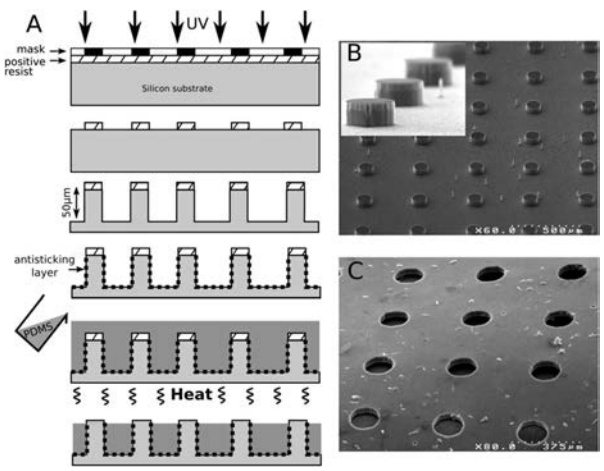

Fig. 6 Fabrication of a PDMS membrane to make adhesive patterns on the gels. (A) Technological steps to make the PDMS membrane. (B) SEM image of the silicon mold of 100 μm diameter cylinders. (C) SEM image of the PDMS membrane for 150 μm islands.

used the 2D particle image velocimetry (PIV) toolbox MatPIV written for Matlab to calculate the bead displacement field. PIV was performed on a plane 1 μm below the cell surface with a window size of (64 × 64) pixels (*i.e.* 6.4 × 6.4 μm) and a 50% overlap between windows. We used a median filter to remove the very few aberrant vectors whose deviation from the neighboring ones was greater than twice the standard deviation in the neighboring area. The forces were calculated using this displacement field using regularization techniques as in ref. 32 and using the L-curve criterium for the choice of the regularization parameter.

6.8 Data analysis

Data analysis was performed using home made programs in Matlab language (The MathWorks, Natick, MA).

- Single cell: orientation bundle:

To get the orientation of the actin bundle on single cells, we used the same methodology used by Bosveld *et al.* to get the anisotropy of the D:GFP signal distribution.[41] Shortly, we performed a fast Fourier transform (FT) on each sub-image (size 96 × 96 pixels, overlap 66%) from the whole actin image using Matlab's built-in function fft2.m. In order to reduce spectral artifacts, the raw image was multiplied by a square cosine before computing its FT. The FT's norm was a function of the Fourier reciprocal space coordinates, $F(\tilde{x},\tilde{y})$, corresponding to a distribution of gray levels. It was maximal at the center, $(\tilde{x},\tilde{y}) = (0,0)$ and decreased faster in the direction of the actin pattern anisotropy than in the orthogonal direction. This function was binarized by keeping the bigger region $(\tilde{x},\tilde{y})$, having gray levels above the 90th percentile. We calculated its variance matrix $\begin{pmatrix} \overline{\tilde{x}^2} & \overline{\tilde{x}\tilde{y}} \\ \overline{\tilde{x}\tilde{y}} & \overline{\tilde{y}^2} \end{pmatrix}$.

The traceless part of this matrix had two opposite eigenvalues $\pm\mu$: here $|\mu|$ quantified the variance of actin pattern anisotropy, so that $\sqrt{|\mu|}$ quantified its standard deviation. The eigenvector with a negative eigenvalue typically reflected the direction of the actin pattern anisotropy.

- Finite sized cell assemblies were analyzed as follows. A binary mask delineating the contour of the cell assembly was created using the ImageJ open license software (NIH, Bethesda). Data out of the mask were set to zero. A regular mesh was generated in cylindrical coordinates, centered in the mask. We used an optimal sampling of 32 pixels for the radius and $\pi/30$ rad for the angle. The cylindrical grid was then converted to Cartesian coordinates. The data, obtained from PIV on a regular Cartesian grid, were interpolated on this new Cartesian mesh, now of variable mesh size. The angular cross-correlation function (eqn (7)) was computed on this mesh using the Matlab *crosscorr* function modified to include periodic boundary conditions. The direction-averaged cross-correlation function, eqn (6), was computed using the Matlab *xcorr2* function on the original dataset extracted from the mask. Creating a regular, cylindrical mesh and interpolating the data on its Cartesian analog optimize the relevance of the interpolation. Nevertheless, we could not avoid the irrelevance of the interpolation close to the center of the mask, where the number of data points is too limited. For this reason, only results for radius larger than 96 pixels are considered.

- Statistics: correlation lengths of displacements and stress for single cells are the result of the average over 6 time lapses on one cell. Data on finite sized cell assemblies were obtained from single-field images (1344 × 1024 pixels). Statistics was performed either by averaging the data on 2 time lapses, separated by 15 min, or by analyzing the dispersion of the results on individual experiments. Data from the analysis of monolayers were obtained from 4 field images (2560 × 2160 pixels). Statistics was performed by averaging the results obtained from 16 sliding windows of 1024 × 1024 pixels. Fits were performed using log-normal distributions, that is appropriate to describe uncorrelated data constrained to be positive. Error bars on correlation lengths are evaluated using the *nlparci* function of Matlab.

Acknowledgements

The authors acknowledge the financial support from Region Rhône Alpes (Cible2010) and Agence Nationale de la Recherche (ANR-12-JVSE5-0008-01).

References

1 D. Verma, N. Ye, F. Meng, F. Sachs, J. Rahimzadeh and S. Z. Hua, *PLoS One*, 2012, **7**, e44167.
2 L. B. Hazeltine, C. S. Simmons, M. R. Salick, X. Lian, M. G. Badur, W. Han, S. M. Delgado, T. Wakatsuki, W. C. Crone, B. L. Pruitt and S. P. Palecek, *Int. J. Cell Biol.*, 2012, **2012**, 508294.
3 X. Yao, R. Peng and J. Ding, *Adv. Mater.*, 2013, **25**, 5257–5286.
4 F. Twiss and J. de Rooij, *Cell. Mol. Life Sci.*, 2013, **70**, 4101–4116.
5 S. A. Ruiz and C. S. Chen, *Stem Cells*, 2008, **26**, 2921–2927.
6 X. Yao, R. Peng and J. Ding, *Biomaterials*, 2013, **34**, 930–939.
7 F. Meng and F. Sachs, *J. Cell Sci.*, 2012, **125**, 743–750.
8 N. Borghi, M. Sorokina, O. G. Shcherbakova, W. I. Weis, B. L. Pruitt, W. J. Nelson and A. R. Dunn, *Proc. Natl. Acad. Sci. U. S. A.*, 2012, **109**, 12568–12573.
9 J. P. Butler, I. M. Tolić-Nørrelykke, B. Fabry and J. J. Fredberg, *Am. J. Physiol.: Cell Physiol.*, 2002, **282**, C595–C605.
10 D. T. Tambe, C. C. Hardin, T. E. Angelini, K. Rajendran, C. Y. Park, X. Serra-Picamal, E. H. Zhou, M. H. Zaman, J. P. Butler, D. A. Weitz, J. J. Fredberg and X. Trepat, *Nat. Mater.*, 2011, **10**, 469–475.
11 D. T. Tambe, U. Croutelle, X. Trepat, C. Y. Park, J. H. Kim, E. Millet, J. P. Butler and J. J. Fredberg, *PLoS One*, 2013, **8**, e55172.
12 R. Krishnan, D. D. Klumpers, C. Y. Park, K. Rajendran, X. Trepat, J. van Bezu, V. W. M. van Hinsbergh, C. V. Carman, J. D. Brain, J. J. Fredberg, J. P. Butler and G. P. van Nieuw Amerongen, *Am. J. Physiol.: Cell Physiol.*, 2011, **300**, C146–C154.
13 M. Théry, *J. Cell Sci.*, 2010, **123**, 4201–4213.
14 R. Peng, X. Yao and J. Ding, *Biomaterials*, 2011, **32**, 8048–8057.

15 M. Théry, V. Racine, M. Piel, A. Ppin, A. Dimitrov, Y. Chen, J.-B. Sibarita and M. Bornens, *Proc. Natl. Acad. Sci. U. S. A.*, 2006, **103**, 19771–19776.
16 Z. Liu, N. J. Sniadecki and C. S. Chen, *Cell. Mol. Bioeng.*, 2010, **3**, 50–59.
17 V. Maruthamuthu, B. Sabass, U. S. Schwarz and M. L. Gardel, *Proc. Natl. Acad. Sci. U. S. A.*, 2011, **108**, 4708–4713.
18 A. Chervin-Pétinot, M. Courçon, S. Almagro, A. Nicolas, A. Grichine, D. Grunwald, M.-H. Prandini, P. Huber and D. Gulino-Debrac, *J. Biol. Chem.*, 2012, **287**, 7556–7572.
19 K. Taguchi, T. Ishiuchi and M. Takeichi, *J. Cell Biol.*, 2011, **194**, 643–656.
20 T. Yeung, P. C. Georges, L. A. Flanagan, B. Marg, M. Ortiz, M. Funaki, N. Zahir, W. Ming, V. Weaver and P. A. Janmey, *Cell Motil. Cytoskeleton*, 2005, **60**, 24–34.
21 A. Saez, M. Ghibaudo, A. Buguin, P. Silberzan and B. Ladoux, *Proc. Natl. Acad. Sci. U. S. A.*, 2007, **104**, 8281–8286.
22 D. E. Ingber, *J. Cell Sci.*, 2003, **116**, 1157–1173.
23 X. Trepat, M. R. Wasserman, T. E. Angelini, E. Millet, D. A. Weitz, J. P. Butler and J. J. Fredberg, *Nat. Phys.*, 2009, **5**, 426–430.
24 S. S. Hur, J. C. del Álamo, J. S. Park, Y.-S. Li, H. A. Nguyen, D. Teng, K.-C. Wang, L. Flores, B. Alonso-Latorre, J. C. Lasheras and S. Chien, *Proc. Natl. Acad. Sci. U. S. A.*, 2012, **109**, 11110–11115.
25 B. Sabass, M. L. Gardel, C. M. Waterman and U. S. Schwarz, *Biophys. J.*, 2008, **94**, 207–220.
26 L. Landau and E. Lifchitz, *Theory of elasticity*, Mir Ed., 1967.
27 A. Nicolas and S. A. Safran, *Phys. Rev. E: Stat., Nonlinear, Soft Matter Phys.*, 2004, **69**, 051902.
28 S. A. Maskarinec, C. Franck, D. A. Tirrell and G. Ravichandran, *Proc. Natl. Acad. Sci. U. S. A.*, 2009, **106**, 22108–22113.
29 S. S. Hur, Y. Zhao, Y.-S. Li, E. Botvinick and S. Chien, *Cell. Mol. Bioeng.*, 2009, **2**, 425–436.
30 H. Delanoë-Ayari, J. P. Rieu and M. Sano, *Phys. Rev. Lett.*, 2010, **105**, 248103.
31 K. M. Stroka and H. Aranda-Espinoza, *Cell. Mol. Bioeng.*, 2011, **4**, 9–27.
32 H. Delanoë-Ayari, S. Iwaya, Y. T. Maeda, J. Inose, C. Rivière, M. Sano and J.-P. Rieu, *Cell Motil. Cytoskeleton*, 2008, **65**, 314–331.
33 D. T. Burnette, S. Manley, P. Sengupta, R. Sougrat, M. W. Davidson, B. Kachar and J. Lippincott-Schwartz, *Nat. Cell Biol.*, 2011, **13**, 371–381.
34 H. Delanoë-Ayari, S. Iwaya, Y. T. Maeda, J. Inose, C. Rivière, M. Sano and J.-P. Rieu, *Cell Motil. Cytoskeleton*, 2008, **65**, 314–331.
35 C. Yan, J. Sun and J. Ding, *Biomaterials*, 2011, **32**, 3931–3938.
36 T. E. Angelini, E. Hannezo, X. Trepat, J. J. Fredberg and D. A. Weitz, *Phys. Rev. Lett.*, 2010, **104**, 168104.
37 N. Wang, I. M. Tolić-Nørrelykke, J. Chen, S. M. Mijailovich, J. P. Butler, J. J. Fredberg and D. Stamenovi, *Am. J. Physiol.: Cell Physiol.*, 2002, **282**, C606–C616.
38 M. Dembo and Y. L. Wang, *Biophys. J.*, 1999, **76**, 2307–2316.
39 N. Wang, E. Ostuni, G. M. Whitesides and D. E. Ingber, *Cell Motil. Cytoskeleton*, 2002, **52**, 97–106.
40 D. Fuard, M. Moussus, C. Tomba, D. Peyrade and A. Nicolas, *J. Vac. Sci. Technol., B: Microelectron. Nanometer Struct.–Process., Meas., Phenom.*, 2010, **28**, C6K1.
41 F. Bosveld, I. Bonnet, B. Guirao, S. Tlili, Z. Wang, A. Petitalot, R. Marchand, P.-L. Bardet, P. Marcq, F. Graner and Y. Bellaïche, *Science*, 2012, **336**, 724–727.